

# New phase and deformation behavior in directional solidified NiTiAl based intermetallic alloy upon cyclic tensile loading - unloading

Zheng, L.J.; Zhang, F.X.; Ding, Rengen; Wang, F.F.; Zhang, H

DOI:

[10.1016/j.matdes.2016.07.149](https://doi.org/10.1016/j.matdes.2016.07.149)

License:

Creative Commons: Attribution-NonCommercial-NoDerivs (CC BY-NC-ND)

*Document Version*

Peer reviewed version

*Citation for published version (Harvard):*

Zheng, LJ, Zhang, FX, Ding, R, Wang, FF & Zhang, H 2016, 'New phase and deformation behavior in directional solidified NiTiAl based intermetallic alloy upon cyclic tensile loading - unloading', *Materials and Design*, vol. 110, pp. 494-502. <https://doi.org/10.1016/j.matdes.2016.07.149>

[Link to publication on Research at Birmingham portal](#)

**Publisher Rights Statement:**

Checked 7/9/2016

**General rights**

Unless a licence is specified above, all rights (including copyright and moral rights) in this document are retained by the authors and/or the copyright holders. The express permission of the copyright holder must be obtained for any use of this material other than for purposes permitted by law.

- Users may freely distribute the URL that is used to identify this publication.
- Users may download and/or print one copy of the publication from the University of Birmingham research portal for the purpose of private study or non-commercial research.
- User may use extracts from the document in line with the concept of 'fair dealing' under the Copyright, Designs and Patents Act 1988 (?)
- Users may not further distribute the material nor use it for the purposes of commercial gain.

Where a licence is displayed above, please note the terms and conditions of the licence govern your use of this document.

When citing, please reference the published version.

**Take down policy**

While the University of Birmingham exercises care and attention in making items available there are rare occasions when an item has been uploaded in error or has been deemed to be commercially or otherwise sensitive.

If you believe that this is the case for this document, please contact [UBIRA@lists.bham.ac.uk](mailto:UBIRA@lists.bham.ac.uk) providing details and we will remove access to the work immediately and investigate.

## Accepted Manuscript

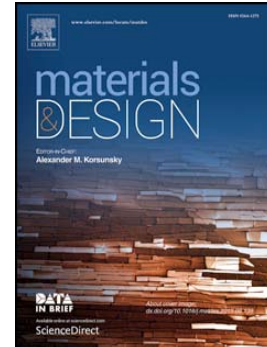
New phase and deformation behavior in directional solidified NiTiAl based intermetallic alloy upon cyclic tensile loading-unloading

L.J. Zheng, F.X. Zhang, R.G. Ding, F.F. Wang, H. Zhang

PII: S0264-1275(16)31056-5  
DOI: doi: [10.1016/j.matdes.2016.07.149](https://doi.org/10.1016/j.matdes.2016.07.149)  
Reference: JMADE 2153

To appear in:

Received date: 20 April 2016  
Revised date: 29 July 2016  
Accepted date: 30 July 2016



Please cite this article as: L.J. Zheng, F.X. Zhang, R.G. Ding, F.F. Wang, H. Zhang, New phase and deformation behavior in directional solidified NiTiAl based intermetallic alloy upon cyclic tensile loading-unloading, (2016), doi: [10.1016/j.matdes.2016.07.149](https://doi.org/10.1016/j.matdes.2016.07.149)

This is a PDF file of an unedited manuscript that has been accepted for publication. As a service to our customers we are providing this early version of the manuscript. The manuscript will undergo copyediting, typesetting, and review of the resulting proof before it is published in its final form. Please note that during the production process errors may be discovered which could affect the content, and all legal disclaimers that apply to the journal pertain.

**New phase and deformation behavior in directional solidified NiTiAl based  
intermetallic alloy upon cyclic tensile loading-unloading**

L.J. Zheng<sup>a</sup>, F.X. Zhang<sup>a</sup>, R.G. Ding<sup>b</sup>, F.F. Wang<sup>a</sup>, H. Zhang<sup>a,1</sup>

<sup>a</sup> School of Materials Science and Engineering, Beihang University, Beijing 100191, China

<sup>b</sup> School of Metallurgy and Materials, The University of Birmingham, Birmingham, B15 2TT, UK

**Abstract:** In the present paper, to understand the nature of newly designed Ni<sub>43</sub>Ti<sub>4</sub>Al<sub>2</sub>Nb<sub>2</sub>Hf alloys in the case of avoiding shape memory, TEM and HREM were used to reveal the precipitation type, phase composition and its relationship with the hardness. Cyclic tensile loading-unloading test is also carried out to study the deformation behavior. It is observed that a new phase with the approximate composition of Ti<sub>36±2</sub>-Ni<sub>34±2</sub>-Nb<sub>20±2</sub>-Al<sub>8±1</sub>-Hf<sub>2±0.5</sub> precipitates in the directional solidified Ni<sub>43</sub>Ti<sub>4</sub>Al<sub>2</sub>Nb<sub>2</sub>Hf alloy, which is identified to be the base-centered monoclinic lattice with lattice parameters  $a = 0.987$  nm,  $b = 0.504$  nm,  $c = 1.172$  nm,  $\alpha = \gamma = 90^\circ$ ,  $\beta = 130.18^\circ$ , and space group C2/c. The hardness of the Ni<sub>36</sub>Ti<sub>20</sub>Nb<sub>8</sub>Al<sub>2</sub>Hf alloy with same composition to the new phase is more than 810 HV, nearly twice of that of the Ni<sub>43</sub>Ti<sub>4</sub>Al<sub>2</sub>Nb<sub>2</sub>Hf alloy, which confirms the strengthening effect of the new phase. In addition, the cyclic loading results indicate that the linear recoverable strain is more than 3%, which exhibits the significantly enhanced load capability of this alloy.

**Key words:** NiTiAl based alloy; Intermetallics; Hardness; Base-centered monoclinic lattice; Cyclic strain-stress response behavior

## 1. Introduction

<sup>1</sup> Corresponding author: Tel: +86-10-82316958, fax: +86-10-82338598, E-mail address: zhanghu@buaa.edu.cn

Over the last decade, intermetallics such as nickel aluminides and titanium aluminides have been considered as potential candidates for high temperature applications [1-2]. However, the combination of good strength and good ductility has generally been a dilemma in these intermetallics. Unlike other B2 intermetallics such as NiAl or FeAl, Stoichiometric NiTi has relatively high room-temperature ductility [3]. Meantime, NiTi alloys have also intrinsically good aqueous corrosion resistance [4]. Therefore, it is thought that an intermetallic alloy based on this phase will have sufficient ductility to be used as structural materials in the case of avoiding shape memory [5-6]. For example, it has been developed as a credible candidate material for spacecraft bearing applications [7].

The addition of 8.43 at% Al into B2 NiTi matrix can enhance the compression strength as high as 2300 MPa at room temperature (RT), which is attributed to fine precipitation of coherent L21 (Heusler)-Ni<sub>2</sub>TiAl compound phases in a NiTiAl matrix [8]. Hence, the Ni<sub>2</sub>TiAl ( $\beta'$ ) and B2-NiTi ( $\beta$ ) phase might be expected to form a precipitation hardening system with both good mechanical strength and some ductility, which is similar to the conventional  $\gamma/\gamma'$  structure of Ni-base superalloys [9-10]. However, the misfit between the NiTi matrix and Ni<sub>2</sub>TiAl ( $\beta'$ ) precipitates in the Ni-Al-Ti system amounts to about 1.5%, considerably larger than the misfit of a few tenths of percent in  $\gamma/\gamma'$  alloys, that is believed to have a detrimental effect on the creep properties at high temperatures [11-13]. Also, ductility of NiTiAl alloys is gradually reduced as the Al content is increased, as Heusler phase forms primary dendrites, embrittling the material when Al content is above 10.95 at.% [8]. Thus, the compositional control of Al is essential to guarantee the ductility in NiTiAl alloys. In addition, high melting point elements, such as Nb, Hf, Mo and etc, also exhibit the potential in enhancing the integrative mechanical properties at

elevated temperature of NiTiAl alloys. As potential high-temperature structural materials, addition of Nb contributes to the dramatic improvement of oxidation resistance at 1073K in NiTiAlNb alloy [14-15]. Moreover, it is reported that the addition of larger-sized Hf or Mo into the NiTiAl alloy can take effect of solution strengthening and dramatically reinforce the alloy [16-17]. In our previous work, the RT tensile strength of the Nb and Hf modified NiTiAl alloy can be achieved as high as more than 1900 MPa, nearly reaching the level of ultra-high strength steel, and no Heusler phase formation in the alloy [18]. In particular, a new phase has been found in this B2-typed multi-element NiTiAlNbHf alloy, but little is known about the formation, characteristics, role and relationship of this new phase with mechanical property. It is well known that many investigations about NiTi shape memory alloy (SMA) have been focusing on superelasticity or pseudoelasticity behavior and specific properties (transformation temperature, microhardness, indentation modulus) using cyclic loading technology [19-21]. The SMA NiTi with near-equiatom composition may deform by a reversible, thermoelastic transformation between a high-temperature, cubic (B2) parent austenitic phase and a low-temperature, monoclinic (B19' ) martensitic phase [22-24]. However, to the best of our knowledge, no study exists on the mechanical behavior of NiTiAlNbHf alloy where an austenitic matrix deforms without the presence of martensite phase. Without such information, it is not possible to systemically optimize the B2 NiTiAl based alloy for future structural material applications. In the present paper, to understand the nature of NiTiAlNbHf series alloys, TEM and HREM were used to reveal the microstructure in details, especially the new phase, and cyclic tensile loading test is also carried out to study its relationship with the mechanical property.

## 2. Experimental procedure

## 2.1. Processing

The nominal composition of the alloy used in the present study is Ni<sub>43</sub>Ti<sub>4</sub>Al<sub>2</sub>Nb<sub>2</sub>Hf (at%). Master ingots were made from pure elements (99.76 wt% Ti, 99.98 wt% Ni, 99.99 wt% Al, 99.98 wt% Nb and 99.9 wt% Hf) in a water-cooled copper crucible arc-melting furnace under argon atmosphere. To ensure composition homogeneity, the ingots were melted four times. Before the DS experiment, the bar stock for DS was cut by wire-electrode cutting to 14 mm in diameter and 220 mm in total length from the master alloy ingots. After grinding, cleaning and drying, the bars were enclosed in a home-made Y<sub>2</sub>O<sub>3</sub>/Al<sub>2</sub>O<sub>3</sub> double layer ceramic tube, which was 240 mm in length, 20 mm in outer diameter and 14.5 mm in inner diameter [25]. The DS experiments were carried out in a vertical Bridgman furnace with W-cylinder heating and liquid metal cooling. Before the DS experiments, the chamber of the furnace was evacuated at a 10<sup>-3</sup> Pa level and backfilled with high purity argon to a pressure of 0.05 MPa. Then, the furnace was heated to 1550 °C to melt the alloy. After reaching the holding time of 20 min, the ceramic tube and the melt inside were drawn into the Ga-In-Sn cooling liquid.

## 2.2. Microstructural studies

The microstructural samples were sampled from the centers of the DS bar stock, which are the steady-state growth regions. The samples were cut in transverse section and then ground and polished. The microstructure and phase compositions were examined using a JXA8100 electro-probe microanalyzer (EPMA), which was equipped with energy dispersive X-ray spectroscopy (EDS). The phase types were analyzed with a D/MAX-2500 X-type X-ray diffractometer (XRD) with Cu K $\alpha$  radiation (voltage: 40 kV; current: 200 mA; scanning speed

of 6°/min; scanning range of 10–90°). Thin foils for transmission electron microscopy (TEM) observation were prepared using the argon ion thinning technique. The TEM imaging and selected area diffraction pattern (SADP) were performed on a JEOL-2100F electron microscope. EDS was also performed on the JEOL 2100F TEM operating at 200 kV and equipped with a Schottky field-emission gun (FEG) and an Oxford ultrathin-window EDS detector.

### 2.3. Hardness and Cyclic loading test

Vickers hardness measurements were carried out on polished sample surface. 980 mN load was applied for 15 s using a diamond Vickers indenter (FM800, Japan). More than five indents were performed on each sample, and average hardness values were achieved among these five indents. The tensile loading specimens were in the gauge size of 18mm×3mm×2mm. The tensile direction is parallel to the directional solidification growth direction. The tensile loading tests were carried out using an SANS-CMT5504 test machine. Axial strain was measured using an YYJ-2/10 type extensometer. The cyclic tensile loading is at a speed of 0.05mm/min.

## 3. Results and discussion

### 3.1. The precipitates in the DS Ni<sub>43</sub>Ti<sub>4</sub>Al<sub>2</sub>Nb<sub>2</sub>Hf based alloy

Fig. 1(a) show the typical microstructure of directional solidified Ni<sub>43</sub>Ti<sub>4</sub>Al<sub>2</sub>Nb<sub>2</sub>Hf (at%) alloys, the phases details in the interdendritic area is magnified in Fig. 1(b). It can be indicated that the microstructure consisted of grey matrix, dark second phase, white second phase, light grey phase which is adjacent to the dark and white phases. These phase morphologies are the same as the results investigated by Pan LW et al [16]. But, in order to quite appropriate to study the composition of each phase, here, accurate TEM-EDS spectra collected from each contrast have

been carried out and corresponding datum are shown in Fig.1c-f.

Quantitative TEM-EDS data indicates that the composition of matrix with grey contrast is the near equi-atomic NiTi matrix phase, in which small amounts of Al, Hf and Nb are dissolved. In addition, the black one represents the  $Ti_2Ni$  phase, while the white region distributes  $\beta$ -Nb phase with Nb content as high as up to 76.74 at%. The SAED patterns of  $Ti_2Ni$  and  $\beta$ -Nb phases are shown in Fig.2. As reported by Meng et al. [15], the  $Ti_2Ni$  phase can strengthen the NiTi matrix phase at room temperature. Zhang et al. [26] thought that the  $\beta$ -Nb phase is a plasticity phase, whereas the  $Ti_2Ni$  phase is a brittleness phase at room temperature. As for the composition of light grey region, which has been once thought to be the same as the white  $\beta$ -Nb phase but more Al, Ti, Hf and Ni atoms dissolved, equivalently  $\beta$ -Nb (Ti, Ni, Al, Hf) phase [27-28]. In the present work, more detailed and accurate observation about this phase has been done. First, it is determined with a relatively stable composition of  $36 \pm 2$  at% Ti,  $34 \pm 2$  at% Ni,  $20 \pm 2$  at% Nb,  $8 \pm 1$  at% Al and  $2 \pm 0.5$  at% Hf, which is namely X phase for simple. In order to observe each element's distribution intuitively, the EDS element maps are performed, as seen in Fig.3. Distinct phase boundaries can be observed between X phase and dark  $Ti_2Ni$  or white  $\beta$ -Nb phases. In Comparison with  $Ti_2Ni$  and  $\beta$ -Nb phases, an obvious difference is that more Al dissolved in X phase, in addition to this, much less Nb content compared with the  $\beta$ -Nb phases. Actually, viewed X phase at a higher magnification by TEM, it is also found that X phase has totally different lattice structure from  $Ti_2Ni$  and  $\beta$ -Nb, or any other existing phase in the Ni-Ti-Al-Nb-Hf series alloy. Based on the above observation, it has been possible to deduce that X phase is previously unreported in the NiTi based alloy. Thus, it is necessary to make clear of the details of X phase.

### 3.2. The structure of the X phase



Because X phase is large enough to make a SAED study from a single precipitate, hence, Fig. 4 (a-f) shows a set of diffraction tilt series in six different zone axis orientations acquired from X phase (as shown in Fig. 4(g)). Due to the foil sample from the coarse column grain formed by of directional solidification, it is hard to get a set of SAED patterns (EDPs) covering the whole orientation triangle from  $0^\circ$  to  $90^\circ$ . In the sequence of Fig. 4(a)  $\rightarrow$  (b)  $\rightarrow$  (c), the diffraction spots pair marked by the red arrows and A was kept visible when rotating the sample. Similarly, in the sequences of Fig.4 (a)  $\rightarrow$  (d)  $\rightarrow$  (f), the diffraction spots pair marked by the yellow arrows and B was kept visible during rotating, while in the sequences of Fig. 4(a)  $\rightarrow$  (e), the diffraction spots pair marked by green arrows and C was kept visible during rotating. These EDPs can be indexed a base-centred monoclinic lattice with  $a = 0.9872\text{nm}$ ,  $b = 0.5042\text{nm}$ ,  $c = 1.172\text{nm}$ ,  $\alpha=\gamma=90^\circ$  and  $\beta=130.18^\circ$ . The obtained lattice parameters were then used to calculate the angles between the zone axes shown in Fig. 4. All the experimental and calculated tilting angles ( $\phi_{\text{exp}}$  and  $\phi_{\text{cal}}$ ) between neighboring EDPs are indicated in Table 1. As can be seen from Table 1, the experimental angles between two zone axes  $[U_1V_1W_1]$  and  $[U_2V_2W_2]$  are also in a good agreement with the calculated ones, therefore the crystal structure of X phase was confirmed to be a base-centred monoclinic.

In order to determine the unit cell geometry of X phase, a series of Convergent Beam Electron Diffraction (CBED) and SAED patterns of different orientations was recorded. The first Zone Axis Pattern (ZAP) was indexed as  $[\bar{1}02]$  and the corresponding CBED pattern which has a (2mm) symmetry (Fig. 5(a) and (b)). It can be seen from Table 2 that the (2mm) symmetry of projection Whole Pattern(WP) CBED gives the  $2\text{mm}1_R$  projection diffraction group, which relates to four diffraction groups, namely:  $2\text{m}_R\text{m}_R$ ,  $2\text{mm}$ ,  $2\text{mm}1_R$  (three diffraction group not allowed for

monoclinic lattice) and  $2_Rmm_R$  (corresponding to  $2/m$  point group). The second ZAP was indexed as  $[1\bar{1}2]$  (Fig. 5(c)), projection WP CBED taken along  $[1\bar{1}2]$  show a symmetry of (2) (see Fig. 5(d)), thus it corresponds to the  $21_R$  diffraction groups (see Table 2), which relates to the three diffraction groups of  $2_R$ ,  $21_R$  (both diffraction groups correspond to  $2/m$  point group) and 2 (corresponding to 2 point group). Since a  $(2mm)$  plus a (2) 'net' symmetries are typical of a monoclinic crystal system [29]. It further confirms that the crystal system of X phase is a base-centred monoclinic lattice.

The summary of the point group deduction is presented in Table 3. According to Table 3, three types of zones axis patterns are required to identify the point group for monoclinic. Due to the TEM foil with preferred orientation of  $[001]$  resulted from directional solidification, it is hard to acquire the  $[010]$  ZAP. Taking into account the symmetries of  $[\bar{1}02]$  and  $[1\bar{1}2]$  projections, the point group of the structure of the X phase can be established as  $2/m$ . Based on the abovementioned the base-centred monoclinic of X phase,  $2/m$  point group corresponds  $C2/m$  or  $C2/c$  space group. In addition, some diffraction discs in the  $[1\bar{1}2]$  CBED pattern (Fig. 4d) are marked by yellow circles, which exhibit a dark line, which corresponds to a Gjønnes-Moodie (GM) line. Due to the absence of screw axes in a base-centred monoclinic, it is induced the presence of  $c$  glide planes in the X phase. Thus, the correct space group describing the symmetry of the X phase is  $C2/c$ .

HREM observation along the main zone axes of the X phase has revealed some structural details of the precipitate. Figure 6 show the HREM image and the corresponding EDPs. In Fig. 6(a), the  $(200)$ ,  $(110)$  and  $(\bar{1}10)$  lattice planes are marked which correspond to spots  $(200)$ ,  $(110)$  and  $(\bar{1}10)$  respectively in the EDP along  $[001]$  direction (as shown in the inset of Fig. 6(a)).

Similarly, the other HREM images and the corresponding EDPs along  $[1\bar{1}2]$ ,  $[011]$  and  $[012]$  directions are seen in Fig. 6(b), (c) and (d) and the right top corners figures. The different planes spacing are measured from HREM results, and all the lattice planes from HREM results are found to be coincident with the crystal lattice of X phase, which further confirm the base-centred monoclinic of this phase.

### 3.3. Role of X phase on the hardness

According to Pan et al, the ultra-high RT tensile strength can be achieved, even more than 1900 MPa in this alloy, owing to the presences of the  $Ti_2Ni$  and  $\beta-Nb$  phases [15-16,18]. But it is not yet clear about the role of X phase on the mechanical behavior in this alloy. So, in order to evaluate the hardness of the new phase, we specially design and fabricate a new alloy with the X phase composition, using arc-melting furnace with the same processing parameters to the present master alloy. The nominal composition of this new alloy is  $Ni_{36}Ti_{20}Nb_{8}Al_{2}Hf$  (at%), for simple, which is namely 20Nb alloy. Fig. 7(a) shows the microstructure of the arc-casting 20Nb alloy and the corresponding XRD results is shown in Fig. 7(b). It is seen from Fig. 7(a) that the microstructure of the 20Nb alloy comprised of most grey phase, accompanied by dark grey  $B2-NiTi$ , white  $\beta-Nb$  and a few dark  $Ti_2Ni$  particles (as shown in the inset of Fig. 7(a)). The TEM-SAED pattern shown in Fig. 7(c-d) confirms that the grey phase is just the above-mentioned X phase. In addition, due to remarkable increase in the volume fraction of light grey X phase, the  $B2-NiTi$  phase is not distributed continuously any more, and the X phase changes to be the matrix phase. Although the phase morphology of 20Nb alloy is apparently different from that of  $Ni_{43}Ti_{4}Al_{2}Nb_{2}Hf$  alloy, each phase composition is exactly the same as that of  $Ni_{43}Ti_{4}Al_{2}Nb_{2}Hf$  alloy, as can be seen from the EDS results (Table. 4). According to the XRD results (Fig. 7(b)),

there are four phases distributed in the Nb20 alloy, which is consistent with the observation by SEM. For comparison, Fig. 8 gives the Vickers hardness of two alloys. The hardness of the arc-melted Ni<sub>43</sub>Ti<sub>4</sub>Al<sub>2</sub>Nb<sub>2</sub>Hf alloy is about 400 HV, after directional solidification, the hardness improves to about 450 HV. By contrast, it is worth noticing that the hardness of 20Nb alloy is about 810 HV, nearly twice of that of the former. It is convincing that the increasing of X phase can prominently enhance the NiTiAl based alloy. More detailed investigation on the 20Nb alloy is being carried out.

#### 3.4. Cyclic strain-stress response behavior

Extensively studies on the cyclic deformation behavior of NiTi SMA have indicated that NiTi possesses the excellent superelasticity or pseudoelasticity, as much as 8% strain, based on the phase transformation between the cubic B2-phase (austenite) and the monoclinic B19' phase (martensite) [30]. However, so far, very few investigations have been performed on the NiTiAlNbHf alloy (B2 austenite structure). And, to the best of our knowledge, no martensitic phase or intermediate R phase occur in the present alloy. Thus, to have a better understanding the phase stability and deformation behavior of this alloy, cyclic tensile loading and unloading test (controlling by strain) has been performed. The uniaxial loading direction is taken along with the growing direction of DS Ni<sub>43</sub>Ti<sub>4</sub>Al<sub>2</sub>Nb<sub>2</sub>Hf alloy.

Fig. 9(a) shows the strain-stress curves of 25 cycles at a constant maximum strain of 2%, it can be seen that the strain-stress curve keeps unchangeable linear relationship. Further increase in the maximum strain of 3% and continuing 10 cycles, it is still remained the linear recoverable strain (superelastic strain) behavior, as shown in Fig. 9(b). Generally, a maximum of overall

deformation strain is less than 1% for traditional structural materials like steel and some intermetallic alloys, such as NiAl, TiAl and etc. However, as evidenced by cyclic tensile tests, the linear recoverable strain is more than 3% in this DS Ni<sub>43</sub>Ti<sub>4</sub>Al<sub>2</sub>Nb<sub>2</sub>Hf alloy, which exhibits the significantly enhanced load capability. Therefore, it is indicated that the present alloy possess the superior performance in combination of high hardness and high levels of superelastic behavior, which can withstand extreme loading conditions without incurring permanent surface damage. In addition, our previous work found that the linear elastic strain can be achieved as high as 4.27%, coupled with the tensile strength of 1972MPa [27]. Though much more research will be required to understand the NiTiAlNbHf material, the results obtained thus far point to a very bright future for many applications where extreme loading is unavoidable.

#### 4. Conclusions

The NiTiAl-based intermetallic alloy with B2 structure was fabricated by directional solidification as a potential candidate for high temperature structural material applications. The detailed microstructure, Vickers hardness and superelasticity deformation behavior of the alloy were studied. The main results can be summarized as follows:

1. In the DS Ni<sub>43</sub>Ti<sub>4</sub>Al<sub>2</sub>Nb<sub>2</sub>Hf alloy, a new phase (named X phase) appears in the interdendritic area, with the composition of about Ti<sub>36±2</sub>-Ni<sub>34±2</sub>-Nb<sub>20±2</sub>-Al<sub>8±1</sub>-Hf<sub>2±0.5</sub> (at%) determined by TEM-EDS technology.
2. The lattice structure of the X phase is identified to be base-centered monoclinic lattice with lattice parameters,  $a = 0.987$  nm,  $b = 0.504$  nm,  $c = 1.172$  nm,  $\alpha = \gamma = 90^\circ$ ,  $\beta = 130.18^\circ$ . The space group of the X structure was determined to be C2/c on the basis of and CBED

observations.

3. The increasing of X phase can prominently enhance the NiTiAl-based alloy. The Vickers hardness of the DS Ni<sub>43</sub>Ti<sub>4</sub>Al<sub>2</sub>Nb<sub>2</sub>Hf alloy is about 450 HV. For comparing the influence of X phase, the hardness of 20Nb alloy with the X phase composition is measured to be more than 810 HV, nearly twice of that of the former.
4. The remarkably recoverable, superelastic strain (above 3%) deformation behavior is exhibited in DS Ni<sub>43</sub>Ti<sub>4</sub>Al<sub>2</sub>Nb<sub>2</sub>Hf alloy with B2 austenite structure, which indicates that the alloy possesses the significantly enhanced load capability.

#### Acknowledgements

The authors acknowledge the financial support of this research by the National Natural Science Foundation of China, under Grant NSFC 51471012.

#### References

- [1] Yamaguchi M, Inui H, Ito K. High-temperature structural intermetallics. *Acta Materialia* 2000; 48(1): 307-22.
- [2] Zhang TB, Wu ZE, Hu R, Zhang F, Kou HC, Li JS. Influence of nitrogen on the microstructure and solidification behavior of high Nb containing TiAl alloys. *Materials and Design* 2016; 103: 100-5.
- [3] Mohri M, Nili-Ahmadabadi M, PouryazdanPanah M, Hahn H. Evaluation of structure and mechanical properties of Ni-rich NiTi/Kapton composite film. *Materials Science & Engineering A* 2016; 668:13-9.
- [4] Vojtěch D, Fojt J, Joska L, Novák P. Surface treatment of NiTi shape memory alloy and its

- influence on corrosion behavior. *Surface & Coatings Technology* 2010; 204: 3895–901.
- [5] Otsuka K, Wayman CM. *Shape memory materials*, 1st ed. Cambridge University Press: London;1998.
- [6] Bendersky LA, Voorhees PW, Boettinger WJ, Johnson WC. The role of elastic energy in the morphological development of a Ni-Ti-Al alloy. *Scripta Metal* 1988; 22(7): 1029-34.
- [7] Hornbuckle BD, Xiao XY , Noebe RD, Martens R, Weaver ML, Thompson GB. Hardening behavior and phase decomposition in very Ni-rich Nitinol alloys. *Materials Science & Engineering A* 2015; 639: 336-44.
- [8] Koizumi Y, Ro Y, Nakazawa S, Harada H. NiTi-base intermetallic alloys strengthened by Al substitution. *Mater Sci Eng A* 1997; 223: 36–41.
- [9] Warren P, Murakami Y, Koizumi Y, Harada H. Phase separation in NiTi-Ni<sub>2</sub>TiAl alloy system. *Materials Science and Engineering A* 1997; 223: 17-20.
- [10] Jung J, Ghosh G, Isheim D, Olson GB. Precipitation of Heusler phase (Ni<sub>2</sub>TiAl) from B<sub>2</sub>-TiNi in Ni-Ti-Al and Ni-Ti-Al-X (X=Hf, Zr) Alloys. *Metallurgical and Materials Transactions A* 2003; 34A (6): 1221-35.
- [11] Zheng LJ, Guo YH, Zhou L, Zhang XL, Zhang H. Microstructural characterization in 7 at% Al-containing NiTi-based alloys. *Rare Metals* 2014; 33(5): 534-40.
- [12] Kumeta T, Enomoto M. Influence of alloying elements on the lattice misfit between  $\beta'$  Ni<sub>2</sub>AlTi and  $\beta_2$  NiTi phases. *Scripta Materialia* 2001; 44: 481-6.
- [13] Peters MA, Humphreys CJ. Misfit control in NiTi/Ni<sub>2</sub>TiAl  $\beta/\beta'$  alloys. In: Nathal MV, Darolia R, Liu CT, Martin PL, Miracle DB, Wagner R, Yamaguchi M, editors. *Structural Intermetallics*, The Mineral, Metals & Materials Society; 1997, p.605-12.

- [14] Xu J, Zhao XQ, Gong SK. The influence of Nb diffusion on the oxidation behavior of TiNiAlNb alloys with different Ti/Ni ratio. *Mater Sci Eng A* 2007; 458: 381–4.
- [15] Meng LJ, Li Y, Zhao XQ, Xu HB. Effect of Nb on strengthening mechanism of Ti rich TiNiAl intermetallics. *Acta Aeronautica Et Astronautica Sinica* 2007; 28(4): 1–4.
- [16] Pan LW, Zheng LJ, Han WJ, Zhou L, Hu ZL, Zhang H. High-temperature tensile properties of a NiTi-Al-based alloy prepared by directional solidification and homogenizing treatment. *Materials & Design* 2012; 39: 192-9.
- [17] Song XY, Li Y, Zhang F. Microstructure and mechanical properties of Nb- and Mo-modified NiTi-Al-based intermetallics processed by isothermal forging. *Materials Science & Engineering A* 2014; 594: 229–34.
- [18] Jiang DW, Zheng LJ, Zhou L, Pan LW, Tang XX, Zhang H. High temperature tensile properties of directionally solidified Ni-43Ti-4Al-2Nb-2Hf alloy. *Rare Metals* 2012; 31(4): 328-31.
- [19] Polatidis E, Zotov N, Bischoff E, Mittemeijer EJ. The effect of cyclic tensile loading on the stress-induced transformation mechanism in superelastic NiTi alloys: an in-situ X-ray diffraction study. *Scripta Materialia* 2015;100: 59–62.
- [20] Xie X, Kan QH, Kang QZ, Lu FC, Chen KJ. Observation on rate-dependent cyclic transformation domain of super-elastic NiTi shape memory alloy. *Materials Science and Engineering A* 2016; 671(1): 32-47.
- [21] Pelegrina JL, Yawny A, Olbricht J, Eggeler G. Transformation activity in ultrafine grained pseudoelastic NiTi wires during small amplitude loading/unloading experiments. *Journal of Alloys and Compounds* 2015; 651: 655–65.



- [22] Guo W, Kato H. Submicron-porous NiTi and NiTiNb shape memory alloys with high damping capacity fabricated by a new top-down process. *Materials & Design* 2015; 78: 74-9.
- [23] Santamarta R, Arróyave R, Pons J, Evirgen A, Karaman I, Karaca HE, et al. TEM study of structural and microstructural characteristics of a precipitate phase in Ni-rich Ni-Ti-Hf and Ni-Ti-Zr shape memory alloys. *Acta Materialia* 2013; 61: 6191-206.
- [24] Shahmir H, Nili-Ahmadabadi M, Naghdi F. Superelastic behavior of aged and thermomechanical treated NiTi alloy at  $A_f + 10^\circ\text{C}$ . *Materials & Design* 2011; 32: 365-70.
- [25] Zhang HR, Tang X, Zhou L, Gao M, Zhou C, Zhang H. Interactions between Ni-44Ti-5Al-2Nb-Mo alloy and oxide ceramics during directional solidification process. *Journal of Materials Science* 2012; 47: 6451-58.
- [26] Zhang CS, Zhao LC, Duerig TW, Wayman CM. Effects of deformation on the transformation hysteresis and shape memory in a  $\text{Ni}_{47}\text{Ti}_{44}\text{Nb}_9$  alloy. *Scripta Metall Et Mater* 1990; 24:1807-12.
- [27] Pan LW, *Microstructure and Mechanical Properties of Directionally Solidified Ni-Ti-Al-Nb-Hf Alloy*. Beihang University; Beijing: 2012, p. 93 [in Chinese].
- [28] Sang YR, Zheng LJ, Pan Q, Zhou L, Li Y, Zhang H. Microstructural characteristics of directionally solidified Ni-43Ti-4Al-2Nb-2Hf alloy. *Rare Metal* 2011; 30: 340-4.
- [29] Rong YH. *Introduction to analytical electron microscopy*, 1st ed. Higher education press: Beijing; 2006.
- [30] Micklich JP, Ghisleni R, Simon T, Somsen C, Michler J, Eggeler G. Orientation dependence of stress-induced phase transformation and dislocation plasticity in NiTi shape memory alloys on the micro scale. *Materials Science and Engineering A* 2012; 538: 265-71.

**Captions of Tables:**

**Table. 1** Experimental and calculated angles  $\Phi_{\text{exp}}$  and  $\Phi_{\text{cal}}$  between zone axes  $[U_1V_1W_1]$  and  $[U_2V_2W_2]$ .

**Table. 2** Projection WP CBED symmetries of diffraction groups.

**Table. 3** Relation between the relevant diffraction groups and monoclinic crystal point groups.

**Table. 4** TEM-EDS results of each phase in 20Nb alloy.

**Captions of Figures:**

Fig.1. Typical cross-section microstructure of DS Ni<sub>43</sub>Ti<sub>4</sub>Al<sub>2</sub>Nb<sub>2</sub>Hf alloy (a) and enlarged interdendritic area (b), EDS spectra of NiTi (c),  $\beta$ -Nb phase (d), Ti<sub>2</sub>Ni phase (e) and new phase (f).

**Fig. 2** SAED patterns of  $\beta$ -Nb phase (a,b,c) and Ti<sub>2</sub>Ni phase (d,e,f) in DS Ni<sub>43</sub>Ti<sub>4</sub>Al<sub>2</sub>Nb<sub>2</sub>Hf alloy.

**Fig. 3** Morphologies of the interdendritic phases (a) and EDS element map for Ti (b), Nb (c), Ni (d), Al (e) and Hf (f) from the same area.

**Fig. 4** Series of SAED patterns at different zone axes. In the sequence of (a)  $\rightarrow$  (b)  $\rightarrow$  (c), the diffraction spots pair (marked by the red arrows and A) was kept visible when rotating the sample. Similarly, in the sequences of (a)  $\rightarrow$  (d)  $\rightarrow$  (f) and (a)  $\rightarrow$  (e), the diffraction spots pair (marked by the yellow arrows and B, green arrows and C) were kept visible during rotating, respectively.

**Fig. 5** First incidence ZA  $[\bar{1}02]$  SAED patterns (a) and CBED (b), second incidence ZA  $[1\bar{1}2]$  SAED patterns (c), and CBED (d).

**Fig. 6** HREM image of DS Ni<sub>43</sub>Ti<sub>4</sub>Al<sub>2</sub>Nb<sub>2</sub>Hf alloy and the corresponding SAED patterns along  $[001]$  (a),  $[1\bar{1}2]$  (b),  $[011]$  (d) and  $[012]$  (d).

**Fig. 7** Microstructure (a) and XRD pattern (b) of 20Nb alloy, and SAED pattern corresponding to

the X phase in 20Nb alloy along [001](c) and [011](d).

**Fig. 8** Average microhardness of the present Ni<sub>43</sub>Ti<sub>4</sub>Al<sub>2</sub>Nb<sub>2</sub>Hf alloy by arc-melting and directional solidification, compared with Nb<sub>20</sub> alloy by arc-melting process.

**Fig. 9** Evolution of stress–strain curves of DS Ni<sub>43</sub>Ti<sub>4</sub>Al<sub>2</sub>Nb<sub>2</sub>Hf alloy during loading–unloading cycling: (a) maximum strain of 2% and 3% (b).

**Table.1**

$U_1V_1W_1$	$U_2V_2W_2$	$\Phi_{\text{exp}}(^{\circ})$	$\Phi_{\text{cal}}(^{\circ})$
001	$\bar{1}04$	8.06	7.82
001	$\bar{1}02$	14.2	14.2
001	$0\bar{1}2$	12.14	12.86
001	$0\bar{1}1$	23.28	24.84
001	$\bar{3}34$	22.41	23.96
001	$\bar{1}33$	22.14	24.34

**Table. 2**

Projection diffraction groups	Corresponding diffraction groups	Projection WP CBED symmetry
$1_R$	$1, 1_R$	1
$21_R$	$2, 2_R, 21_R$	2
$m1_R$	$m_R, m, m1_R$	m
$2mm1_R$	$2m_Rm_R, 2mm, 2_Rmm_R, 2mm1_R$	2mm
$41_R$	$4, 4_R, 41_R$	4
$4mm1_R$	$4m_Rm_R, 4mm, 4_Rmm_R, 4mm1_R$	4mm
$31_R$	$3, 31_R$	3
$3m1_R$	$3m_R, 3m, 3m1_R$	3m
$61_R$	$6, 6_R, 61_R$	6
$6mm1_R$	$6m_Rm_R, 6mm, 6_Rmm_R, 6mm1_R$	6mm

**Table. 3**

Point group	[010]	[U0W]	[UVW]
2/m	21 <sub>R</sub>	2 <sub>R</sub> mm <sub>R</sub>	2 <sub>R</sub>
m	1 <sub>R</sub>	m	1
2	2	m <sub>R</sub>	1

Pratial table taken from [29]

**Table. 4**

Phase	Composition(at%)				
	Al	Ti	Ni	Nb	Hf
NiTi phase	1.73	42.15	52.51	2.14	1.47
X phase	8.99	35.95	34.19	19.31	1.56
$\beta$ -Nb phase	2.96	23.51	2.30	71.23	0
Ti <sub>2</sub> Ni phase	3.09	56.49	34.94	5.15	0.33

Fig. 1

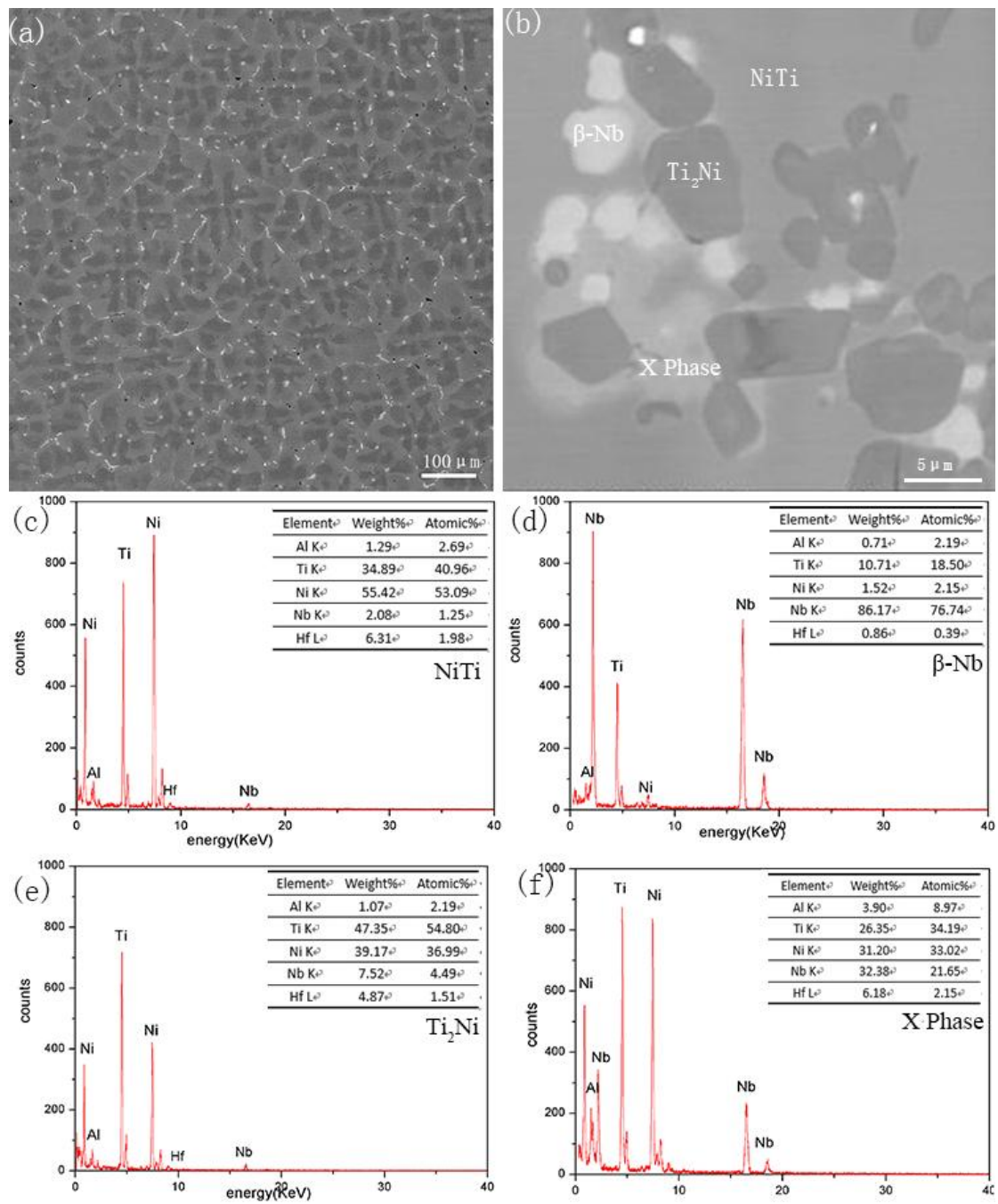




Fig. 2

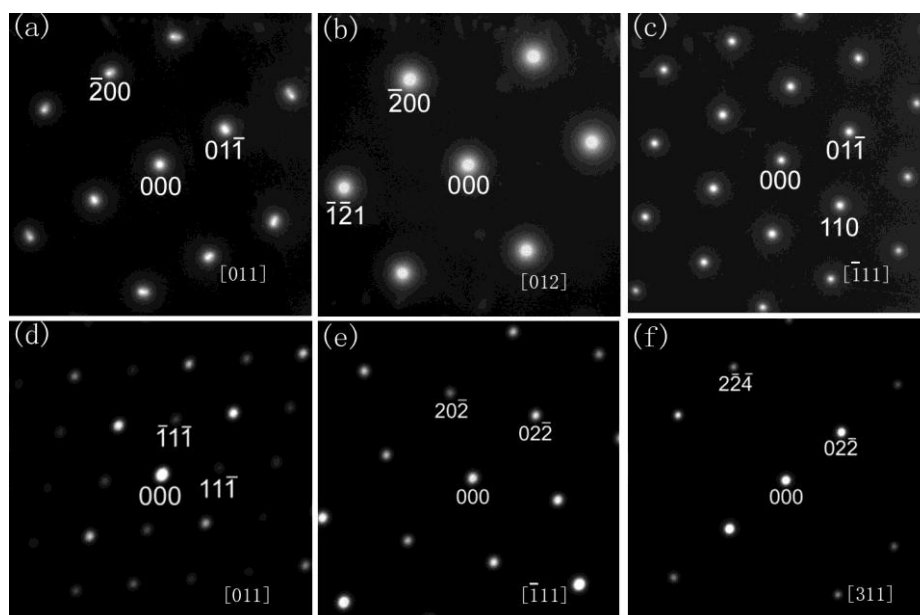


Fig. 3

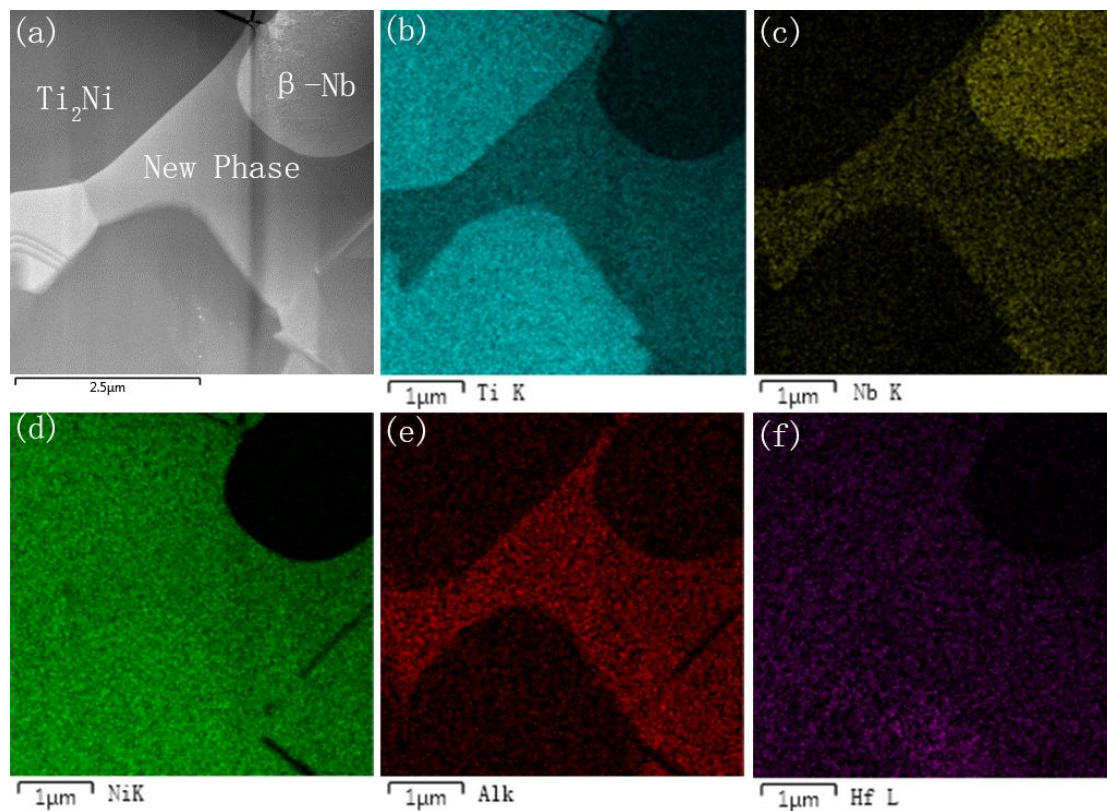


Fig. 4

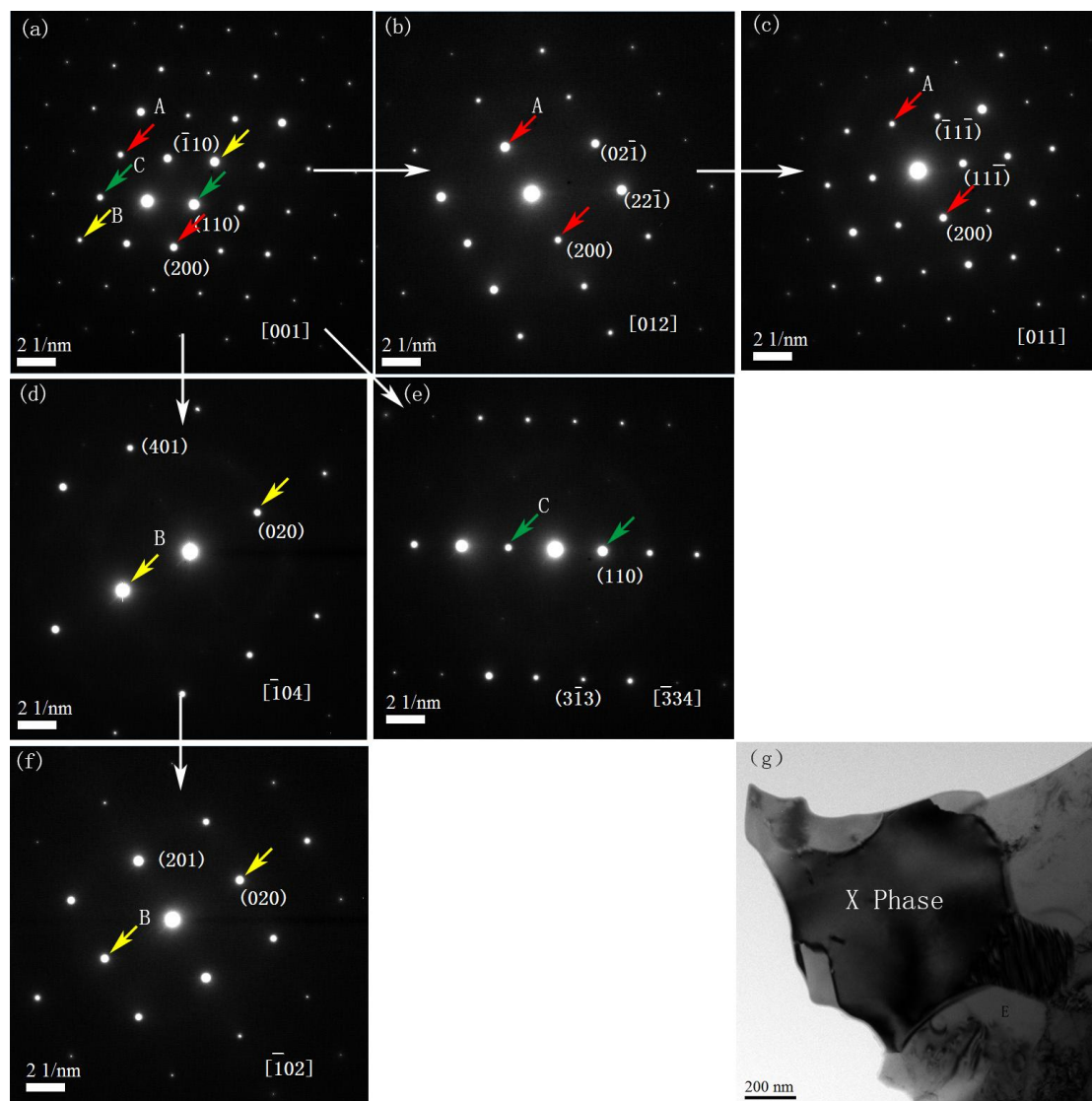


Fig. 5

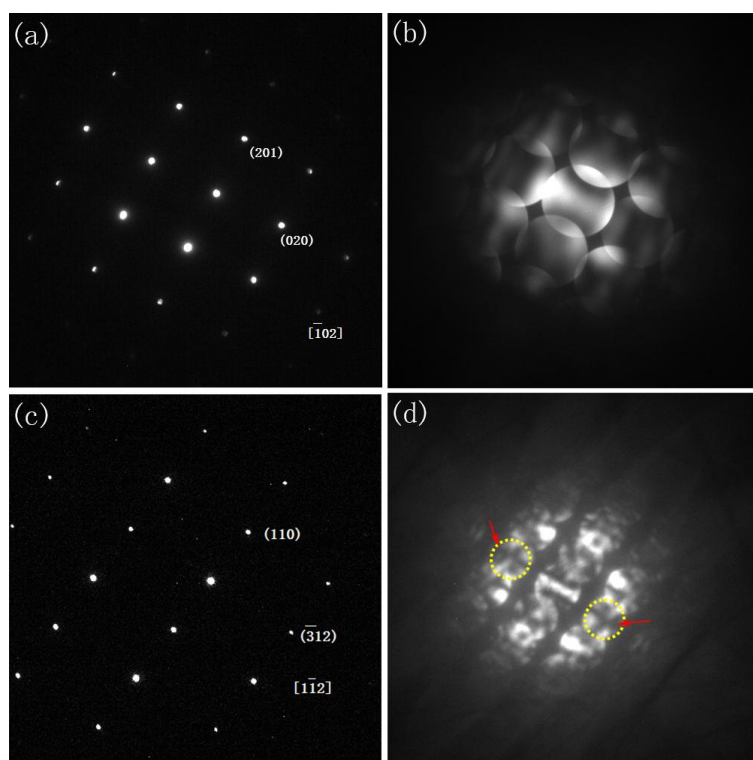


Fig. 6

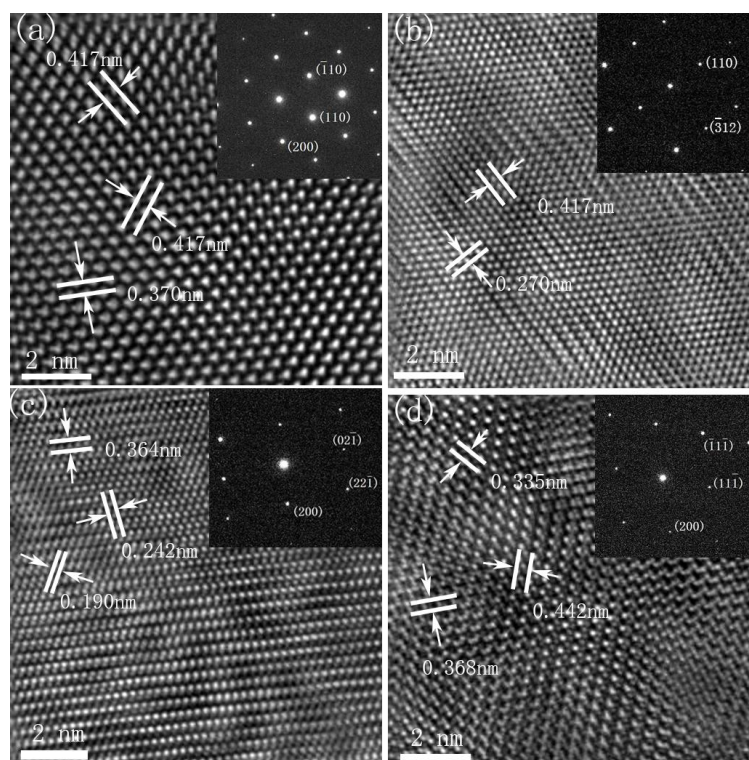


Fig. 7

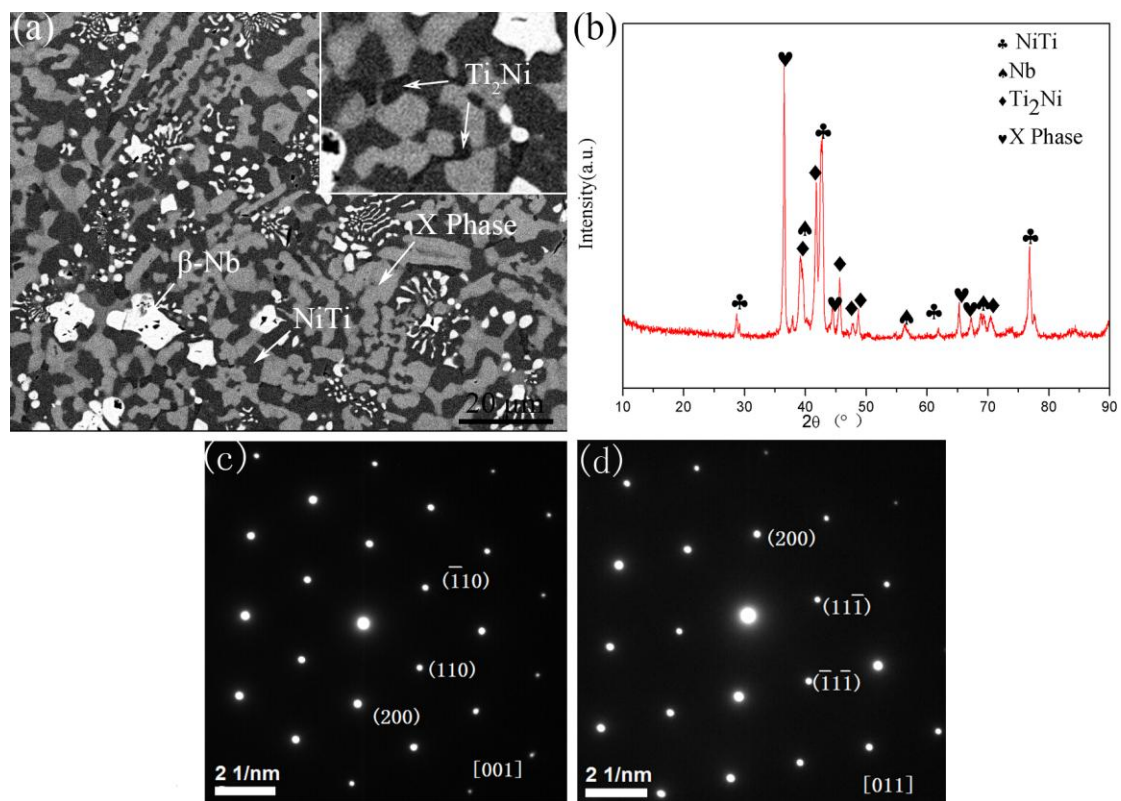


Fig. 8

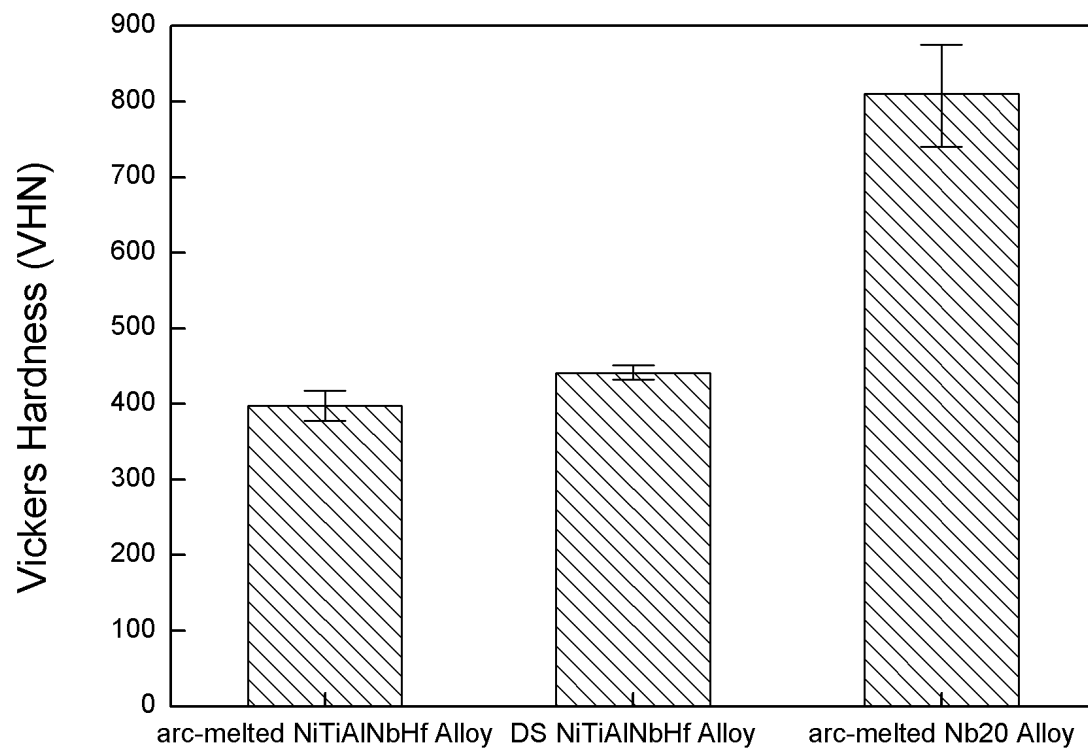
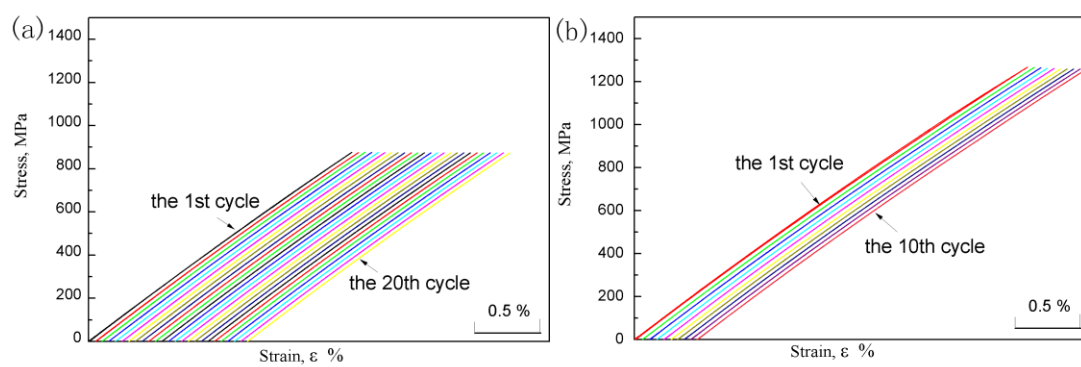
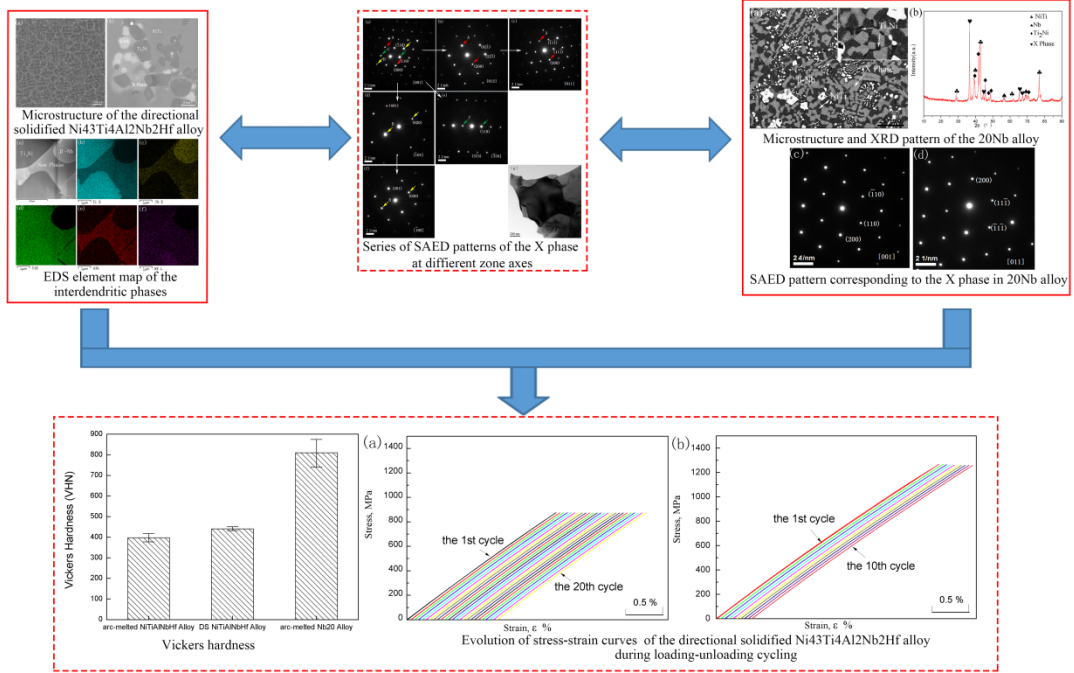




Fig. 9







Graphical abstract

**Highlights**

- The microstructure of directional solidified Ni<sub>43</sub>Ti<sub>4</sub>Al<sub>2</sub>Nb<sub>2</sub>Hf(at%) alloy is comprised of B2-NiTi matrix, Ti<sub>2</sub>Ni phase, β-Nb phase and a new phase with the composition of Ti<sub>36±2</sub>-Ni<sub>34±2</sub>-Nb<sub>20±2</sub>-Al<sub>8±1</sub>-Hf<sub>2±0.5</sub> (at%).
- The new phase is identified to be base-centered monoclinic lattice with lattice parameters, a = 0.987 nm, b = 0.504 nm, c = 1.172 nm, α = γ = 90°, β = 130.18°.
- The new phase dramatically increases the strength of the directional solidified NiTiAl-based alloy.
- The directional solidified Ni<sub>43</sub>Ti<sub>4</sub>Al<sub>2</sub>Nb<sub>2</sub>Hf alloy exhibits remarkably recoverable, superelastic strain (above 3%) deformation behavior.